

Research paper

Resonance and weak chaos in quasiperiodically-forced circle maps

J.D. Meiss ^a*,¹ E. Sander ^b,²^a Department of Applied Mathematics, University of Colorado, Boulder, CO, 80309-0526, USA^b Department of Mathematical Sciences, George Mason University, Fairfax, VA, 22030, USA

ARTICLE INFO

MSC:

37C55

37E10

37E45

65P99

70K43

Keywords:

Circle maps

Quasiperiodic forcing

Arnold tongues

Resonance

Birkhoff averages

Strange nonchaotic attractors

ABSTRACT

In this paper, we distinguish between four categories of dynamics for quasiperiodically-forced (QPF) circle maps: resonant and incommensurate regular dynamics, and strongly and weakly chaotic dynamics, using the weighted Birkhoff average (WBA). Regular orbits can be classified by their rotation vectors, and these can be rapidly computed to machine precision using the WBA. These orbits can be resonant or incommensurate and we distinguish between these by computing their “resonance order,” allowing us to quickly identify and observe the geometric properties of a large set of Arnold tongues. When the dynamics is chaotic the WBA converges slowly. Orbits that are not regular can be *strongly* chaotic, when they have a positive Lyapunov exponent, or *weakly* chaotic when the maximal Lyapunov exponent is not positive. The latter correspond to the strange nonchaotic attractors (SNA) that have been observed in QPF circle maps beginning with models introduced by Ding, Grebogi, and Ott. The WBA provides an efficient new technique to find SNAs, and allows us to accurately compute the proportions of each of the four orbit types as a function of map parameters.

1. Introduction

In this paper we numerically classify four types of dynamics for quasiperiodically-forced (QPF) circle maps. These distinctions allow us to observe patterns in the dynamics for QPF systems as the parameters are changed. The main method we use is the weighted Birkhoff average (WBA), which is an efficient and accurate way to compute Birkhoff (time) averages of a function on phase space. The WBA also allows us to distinguish between regular and chaotic orbits for QPF circle maps. When an orbit is regular, the WBA for the rotation vector converges rapidly and provides a high precision estimate for this vector. This can be used to distinguish between resonant and incommensurate regular orbits and compute an orbit’s rotation vector.

In particular, the WBA can be used to distinguish between orbits that are “weakly”, as opposed to “strongly” chaotic. The former correspond to strange nonchaotic attractors (SNA), i.e., geometrically “strange” attractors that have nonpositive Lyapunov exponents [1–4]. In the classic examples [5,6], SNAs exhibit sensitive dependence on initial conditions but not exponential divergence [7]. We refer to such dynamics as *weak chaos*, as opposed to *strong chaos*, where the orbit has at least one positive Lyapunov exponent. It was previously shown in [8] that the WBA identifies SNAs for the QPF damped pendulum model of [6], and here we use it to distinguish between weak and strong chaos for QPF circle maps. With this classification, we can much more easily compute the location and proportion of such orbits as the parameters vary.

Our paper proceeds as follows: we recall some of the theoretical background and previous results for torus maps in Section 2. The numerical methods that we developed in [9,10] are recalled in Section 3: Section 3.1 explains how to use the WBA to compute

* Corresponding author.

E-mail addresses: jdm@colorado.edu (J.D. Meiss), esander@gmu.edu (E. Sander).¹ JDM was supported in part by the Simons Foundation under Award 601972. Useful conversations with Nathan Duignan are gratefully acknowledged.² ES was supported in part by the Simons Foundation under Award 636383. Both authors would like to thank the referee for their comments and suggestions.

rotation vectors and how it gives an efficient method to identify chaos. In Section 3.2 we recall the method of “resonance orders” to distinguish resonant (lower-dimensional) invariant tori from those that are nonresonant (full-dimensional). We apply these techniques in Section 4 to classify the orbits of two-dimensional torus maps with a rigidly rotating second component. In Section 5 we show how the WBA and Lyapunov exponents can be used together to distinguish strongly chaotic orbits from those that are weakly chaotic. In Section 6 we compute the proportions of the four categories of orbits — resonant, incommensurate, weakly chaotic and strongly chaotic — as a function of the parameters of the map. We conclude in Section 7.

2. Quasiperiodically-forced circle maps: Background

We begin by recalling some of the theoretical background for torus maps, $f : \mathbb{T}^d \rightarrow \mathbb{T}^d$. If $\pi : \mathbb{R}^d \rightarrow \mathbb{T}^d$ is the standard projection, then a map $F : \mathbb{R}^d \rightarrow \mathbb{R}^d$ is a *lift* of f if

$$\pi \circ F = f \circ \pi.$$

Here we take the periods of the torus to be one, so that $F(x) \bmod 1 = f(x \bmod 1)$. We will assume that f is homotopic to the identity; in this case $F(x+m) = F(x)+m$ for each $m \in \mathbb{Z}^d$, i.e., the map has degree one. Note that any two lifts, say F_1 and F_2 , differ by an integer vector, $F_1(x) = F_2(x) + m$ —indeed this must be true for any fixed x , but by continuity the same vector m must work for all x .

In general we can assume that a degree-one torus map has the form

$$x' = f(x) = x + \Omega + g(x; a) \bmod 1, \quad (1)$$

where $\Omega \in \mathbb{T}^d$, a is a parameter vector, and g is periodic, $g(x+m; a) = g(x; a)$ for any $m \in \mathbb{Z}^d$ and every a . The simplest case is Arnold’s circle map, where $d = 1$, and

$$g(x; a) = \frac{a}{2\pi} \sin(2\pi x).$$

The orbit of $x \in \mathbb{T}^d$ under (1) has (pointwise) rotation vector $\omega \in \mathbb{T}^d$ if the limit

$$\omega(x, f) = \lim_{t \rightarrow \infty} \frac{F^t(x) - x}{t} \bmod 1 \quad (2)$$

exists. This is independent of the choice of lift; however, it can depend upon the initial point. When a circle map is a homeomorphism, e.g., $|g'(x; a)| \leq 1$ for all $x \in \mathbb{T}^1$, Poincaré proved that strict monotonicity implies that the limit (2) exists and is independent of x . Moreover, it was shown by Herman that the resulting rotation number ω is a nondecreasing function of Ω . When a circle map f is an increasing diffeomorphism, $f'(x) > 0$, Denjoy showed that when ω is irrational the dynamics of f is topologically conjugate to a rigid rotation. More generally when (1) is a homeomorphism on \mathbb{T}^d , every orbit has the same rotation vector [5]. These results can be found in textbooks such as [11,12].

Here, we will study quasiperiodically-forced (QPF) circle maps, where $d = 2$ and the second component of the map (1) is a rigid rotation in x_2 (i.e., the second component of g , $g_2 = 0$), so that the map is then a skew product:

$$f(x_1, x_2) = (x_1 + \Omega_1 + g_1(x_1, x_2), x_2 + \Omega_2). \quad (3)$$

We still allow the first component, g_1 , to be a general function of both variables x_1 and x_2 . The result is QPF when the second component of Ω is irrational: $\Omega_2 \in \mathbb{R} \setminus \mathbb{Q}$. Our motivation for considering this class of maps is that, though they are two-dimensional, their dynamics is not as complex as the general, two-dimensional case. Nevertheless, QPF circle maps can exhibit both strong and weak chaos, as we will discuss below.

In our calculations we will use the commonly studied extension of the Arnold map, where f is of the form in (3) with

$$g_1(x_1, x_2) = \frac{1}{2\pi} (a_1 \sin(2\pi x_1) + a_2 \sin(2\pi x_2)). \quad (4)$$

The rotation vector (2) for these maps has the property that

$$\omega_2(x, f) = \Omega_2 \quad (5)$$

since the second component is trivial. We will fix Ω_2 to be the inverse of the golden mean in Section 4, and investigate the dependence of ω_1 on the three parameters a_1 , a_2 , and Ω_1 . For the simplest case $a_1 = 0$, and

$$\omega_1 = \lim_{t \rightarrow \infty} \frac{1}{t} \left(t\Omega_1 + \frac{a_2}{2\pi} \sum_{j=0}^{t-1} \sin(2\pi(j\Omega_2 + x_2(0))) \right) = \Omega_1, \quad (6)$$

since the trigonometric terms average to zero. Thus for $a_1 = 0$, $\omega(x, f) = \Omega$ for any a_2 and any x .

Quasi-periodically forced circle maps have been studied in [1,3,13–16], and many of the results are reviewed and extended in [4]. Herman showed that whenever a skew product map on \mathbb{T}^2 is a homeomorphism, then every orbit has a rotation number that depends continuously on f and moreover that the limit (2) is independent of x [5,14]. The case (3) with (4) is a homeomorphism whenever $|a_1| \leq 1$, and in this case the graph $(\omega_1(x, f) : \Omega_1 \in \mathbb{R})$ for fixed a_1 , a_2 , and Ω_2 , is monotone increasing [17].

Maps of the form (3) with (4) can have strange nonchaotic attractors (SNA), i.e., geometrically “strange” attractors that have nonpositive Lyapunov exponents. These attractors have been studied both theoretically and numerically in previous papers. One of the first is [1], which indicated that for fixed a_2 , there are two curves in the (Ω_1, a_1) plane that bound the SNA regime, each of

which is a graph over a_1 . Below the first curve the orbits are quasiperiodic or resonant, and above the second, the dynamics has a positive Lyapunov exponent. In later studies the onset of SNAs has been attributed to the collision of a pair of stable/unstable invariant circles at a dense set of points [3,13,18]. The dynamics on an SNA can be thought of as an orbit that undergoes random transitions between remnants of the colliding circles [2]. In the paper [4] it is shown that when (a_1, a_2) are sufficiently large, SNAs correspond to uncountably many minimal invariant sets.

Using our method for distinguishing weakly chaotic orbits in Section 4, we will see that for each fixed (a_1, a_2) , the set of Ω_1 values for which there is an SNA appears to be a Cantor set. As was seen in [1], the SNAs appear just below, and disappear just above, $a_1 = 1$ (see e.g., Fig. 4). Our technique allows computing the SNAs over a wide parameter regime, and we will see that as a_2 grows the proportion of orbits with SNAs increases (e.g. in Fig. 5 we fix $a_1 = 1.2$ and allow a_2 to vary). We will investigate SNAs further in Section 5.

3. Computational methods

In this section, we recall several of our previously published computational tools that we will adapt to study QPF circle maps in Section 4–5. In Section 3.1 we recall the weighted Birkhoff average (WBA), which was introduced in [19] and further developed in [9,20–22]. It is well-known that even when a time-average exists, its convergence can be slow. The WBA accelerates the convergence of such averages when the orbit is regular, allowing an efficient, and highly accurate calculation. More generally, the difference between the convergence rates for regular and chaotic orbits of the WBA allows for a quick and accurate distinction between these categories. In Section 3.2 we recall a technique for distinguishing between computed rotation vectors that are numerically incommensurate and commensurate. We developed this method of “resonance orders” in [10] for three-dimensional, volume preserving maps. We will use this in Section 4 to compute the analog of Arnold tongues. Finally, in Section 3.3, we compare these methods to more conventional ones. In particular, we discuss the efficiency and accuracy of Lyapunov exponents and the 0–1 test as compared to WBA for distinguishing orbit types.

3.1. Weighted Birkhoff averages

We now give a brief review of the WBA introduced in [20], and how it can distinguish between regular and chaotic orbits [9,10]. Given a map $f : M \rightarrow M$, recall that the time average of a function $h : M \rightarrow \mathbb{R}$ along an orbit of f is simply

$$B(h)(z) = \lim_{T \rightarrow \infty} \frac{1}{T} \sum_{i=0}^{T-1} h \circ f^i(z), \quad (7)$$

if this limit exists. Under the assumptions that μ is an f -invariant probability measure ($\mu(A) = \mu(f^{-1}(A))$ for any Borel subset A of M), μ is ergodic, and $h \in L^1(M, \mathbb{R})$, then Birkhoff's ergodic theorem implies that

$$B(h)(z) = \langle h \rangle = \int_M h d\mu$$

for μ -almost every z . However, the convergence to this limit is at best as $1/T$ [23] and can be arbitrarily slow [24].

To compute the average efficiently and accurately for a length- T segment of an orbit, we follow [20] and modify (7) using the C^∞ weight function³

$$\Psi(s) \equiv \begin{cases} \exp\left(-\frac{1}{s(1-s)}\right) & s \in (0, 1) \\ 0 & s \leq 0 \text{ or } s \geq 1 \end{cases}.$$

This exponential bump function converges to zero with infinite smoothness at 0 and 1, i.e., $\Psi^{(k)}(0) = \Psi^{(k)}(1) = 0$ for derivatives of all orders, $k \in \mathbb{N}$. The finite-time weighted Birkhoff average (WBA) is then defined by

$$WB_T(h)(z) \equiv \frac{1}{S} \sum_{i=0}^{T-1} \Psi\left(\frac{i}{T}\right) h \circ f^i(z), \quad (8)$$

with the normalization constant

$$S \equiv \sum_{i=0}^{T-1} \Psi\left(\frac{i}{T}\right). \quad (9)$$

As shown in [20], (8) gives the same answer as $T \rightarrow \infty$ as (7); however, for regular orbits it can converge much more quickly. In particular, if the orbit is conjugate to a rigid rotation with a Diophantine rotation vector ω and the map f and function h are C^∞ , then (8) converges faster than any power [21,26]:

$$|WB_T(h) - \langle h \rangle| < \frac{c_k}{T^k}, \quad \forall k \in \mathbb{N}.$$

This super-polynomial convergence, however, is not observed when the orbit is chaotic.

³ Optimal choices for Ψ have recently been explored by Ruth and Bindel using reduced rank extrapolation [25].

Indeed, in previous work on two-dimensional, area-preserving maps [9], we showed that the rate of convergence of the WBA provides an efficient and accurate method to distinguish between chaotic and regular orbits (see Section 3.3). An estimate of the error in the WBA for a given function h and a given time T is the effective number of digits of accuracy:

$$\text{dig}_T = -\log_{10} |WB_T(h)(z) - WB_T(h)(f^T(z))|, \quad (10)$$

i.e., comparing the result for the first T iterates with that for the next T iterates. In [9], we observed that for the 2D Chirikov standard map, dig_T converges rapidly to machine precision for orbits that lie on invariant circles: double precision accuracy ($\text{dig}_T \sim 14$) for most orbits is obtained within $T \approx 10^4$ iterates. However, it converges slowly, or not at all for chaotic orbits. For example, when there is a mixture of regular and chaotic orbits (e.g. at $k = 1.0$), we computed a histogram of dig_{10^4} , [9, Fig. 3]. This shows two peaks, a broader one around $\text{dig}_T = 2$, corresponding to chaotic orbits and a narrower one around $\text{dig}_T = 14$, that corresponds to regular orbits. The latter peak has a small tail over the interval $6 < \text{dig}_T < 13$: for these orbits the average converges more slowly. We found that such orbits typically lie near the boundary of narrow chaotic layers or are periodic with high period within lower-period island chains.

In [10] we used the WBA to study two-tori in a 3D volume-preserving map. To achieve the same accuracy for higher-dimensional invariant sets, it is natural that one needs more iterates. Specifically, for double-precision computations we used $T = 10^6$ [10, Fig 3] to get a dig_T distribution with two well-separated, narrow peaks with only a small fraction of orbits in the range $6 < \text{dig}_T < 10$.

To obtain a criterion distinguishing chaotic and regular orbits, we choose a cutoff value for dig_T , declaring that

$$\text{dig}_T < D_T \Rightarrow \text{"chaotic"}; \quad (11)$$

conversely, all orbits with $\text{dig}_T > D_T$ are “nonchaotic”. In [10] we chose the cutoff $D_{10^6} = 11$ for a 3D map where the tori can be 1D or 2D. This cutoff is conservative in the sense that a chaotic orbit will not be identified as regular, but there is a possibility that a regular orbit will be misidentified as chaotic. This choice has the benefit that the rotation vector of any orbit identified as regular can be computed with high accuracy, and in that paper we were interested in studying the number theoretic properties of the robust tori. For the current paper we use the less strict criterion

$$T = 10^6, \quad D_T = 9, \quad (12)$$

which is still conservative in that chaotic orbits are quite unlikely to be identified as regular.

In addition to providing the distinction between regular and chaotic orbits, the WBA can be used to compute an accurate value of the time average of a function h of interest. In particular, we can compute the rotation vector (2) of an orbit for a torus map of the form (1) using T iterates by

$$\omega_T = WB_T(F(x) - x) = \Omega + WB_T(g(x; a)), \quad (13)$$

with WB defined by (8). If T is large enough and the rotation vector exists, we expect $\omega_T \approx \omega(x, f)$. For the quasiperiodic case, (5) implies that we only need to compute the first component of (13).

3.2. Resonance orders

For a regular orbit of a map on \mathbb{T}^2 , the frequency vector computed in (13) can be rational, commensurate, or incommensurate, corresponding to periodic orbits, invariant circles or invariant tori, respectively. We now describe the method of resonance orders, developed in [10], for distinguishing between these categories.

To estimate whether a computed vector is essentially rational we would ask that $|\omega - \frac{p}{q}| < \delta$ for $p \in \mathbb{Z}^d$, $q \in \mathbb{N}$; When δ is small, this would correspond to finding a rational approximation of the vector ω . For the case $d = 1$, we developed in [9] a method, based on the Farey tree, to compute the smallest denominator q for a given precision δ .

More generally, $\omega \in \mathbb{R}^d$ has a *commensurability* (or is *resonant* or *mode-locked*) if there is an $m \in \mathbb{Z}^d \setminus \{0\}$ and an $n \in \mathbb{Z}$ such that

$$\omega \in \mathcal{R}_{m,n} = \{\alpha \in \mathbb{R}^d : m \cdot \alpha = n\}, \quad (14)$$

i.e., it lies in the codimension-one, resonant plane $\mathcal{R}_{m,n}$. For $d = 2$, the sets $\mathcal{R}_{m,n}$ are lines. We say that ω has *resonance order* M if it satisfies (14) and $M = \|m\|_1$ is the smallest length of such a (nonzero) vector m . Vectors that do not lie in any resonant plane $\mathcal{R}_{m,n}$, for example, $\omega = (\sqrt{2}, \sqrt{5})$, are *incommensurate*.

The *rank* of the resonance for a given ω is the number of independent commensurability vectors m ; i.e., the dimension of the module of resonance vectors. Note that ω is rational only if the rank is d ; commensurabilities that have lower rank are partially resonant, such as the rank-one vector $\omega = (3\sqrt{2}, 2\sqrt{2} - 1)$, which lies in $\mathcal{R}_{m,n}$ for $(m_1, m_2, n) = (2, -3, 3)$ so that $M = 5$.

A vector ω is then *approximately* commensurate if $|m \cdot \omega - n|$ is small; in [10] we developed a method for detecting such commensurabilities. We say that a vector ω is (m, n) -resonant to precision δ if the resonant plane intersects a ball of radius δ about ω :

$$\mathcal{R}_{m,n} \cap B_\delta(\omega) \neq \emptyset. \quad (15)$$

Using the Euclidean norm, the minimum distance between the plane (14) and the point ω is

$$\Delta_{m,n}(\omega) = \min_{\alpha \in \mathcal{R}_{m,n}} \|\alpha - \omega\|_2 = \frac{|m \cdot \omega - n|}{\|m\|_2}. \quad (16)$$

Thus ω is (m, n) resonant to precision δ , whenever $\Delta_{m,n}(\omega) < \delta$, and we call the value

$$M(\omega, \delta) = \min\{\|m\|_1 : \Delta_{m,n}(\omega) < \delta, m \in \mathbb{Z}^d \setminus \{0\}, n \in \mathbb{Z}\}, \quad (17)$$

the *resonance order* of ω .

To understand what resonance orders are “typical,” in [10] we computed the minimal resonance order (17) for a set of equidistributed, random $\omega \in [0, 1]^2$ as a function of the precision δ . The resulting distribution of $\log(M)$, seen in [10, Fig. 8], has a mean and standard deviation

$$\begin{aligned} \langle \log_{10} M(\omega, \delta) \rangle &= -0.334 \log_{10}(\delta) - 0.091, \\ \sigma &= 0.171. \end{aligned} \quad (18)$$

We observed that the standard deviation seems to be essentially independent of δ . This is also true for $d = 1$, as we found in [9]. Our computations inspired Chen and Haynes [27] and more recently Marklof [28,29] to find rigorous results for the resonance order distributions.

Since the cutoff (12) gives rotation number calculations accurate to within 10^{-9} , we choose $\delta = 10^{-9}$ for (17). For this case, (18) implies that $\langle \log_{10} M \rangle = 2.915$. The implication is that we declare a vector to be nonresonant if

$$256 \leq M \leq 2673 \Rightarrow \text{“nonresonant”}, \quad (19)$$

corresponding to $2.407 < \log_{10}(M) < 3.427$, which is a range of approximately $\pm 3\sigma$ about the mean (18). To test this criterion we selected 10^4 uniformly randomly distributed values in $[0, 1]^2$, and found that 1.36% were incorrectly identified as resonant. Note that the distribution of log-orders for random vectors is not symmetric around the mean; in particular, $M < 256$ occurred 1.32% of the time, and $M > 2673$ occurred 0.04% of the time.

We can further categorize the *resonant* orbits (those that fail Criterion (19)) by the rank of the resonance. Rank-two resonant orbits have frequencies on the intersection of a pair of different resonance lines, which implies that the components of ω are rational, see e.g. [10, Fig 7]. For the QPF case we study here, $\omega_2 = \Omega_2$ is irrational; therefore, all resonant orbits will have rank one.

3.3. Related computational methods

There are two standard methods for identifying chaos: a positive Lyapunov exponent [30] and Gottwald and Melbourne’s 0–1 test for chaos [31]. In [9] we showed our the computation of dig_T in (10) gives a distinction that is as accurate but is more efficient than either of these. In each case the WBA declares an orbit to be regular (a true positive) or chaotic (a true negative), almost always, when either of the other two methods is used as the “truth”.⁴ However the WBA is more efficient since the orbit length can be reduced and one does not need to compute the linearization that is needed for the Lyapunov exponent or an auxiliary function needed for the 0–1 test.

Alternative algorithms for computing rotation vectors and sets include [32] for circle maps, the set-based methods in [33] for torus maps, and methods for numerical continuation of invariant tori [34]. The parameterization method can be used to explicitly compute the conjugacy to rigid rotation [35], and the needed rotation vector can be efficiently computed using the WBA [36]. The frequency analysis method of Laskar [37,38] uses a Hann window to give a quadratically convergent Fourier amplitudes to compute rotation vectors. In a series of papers, Villanueva and collaborators use Richardson extrapolation to estimate rotation numbers for analytic circle diffeomorphisms [39–43]. Experimentally, this appears to give super-convergence for Diophantine irrationals, but the convergence has not been rigorously shown. For a comparison of many of these methods to the WBA, see [21,44].

We know of no alternatives to the method of resonance orders for distinguishing between incommensurate and resonant orbits. For example, as far as we know, there is no generalization of the Farey tree result used in [9] to compute (17) efficiently for $d = 1$.⁵ Nevertheless, since there are finitely many $m \in \mathbb{Z}^d$ such that $\|m\|_1 \leq M$, a brute force computation is of course possible for modest values of M ; we gave such an algorithm in [10].

4. Regular and chaotic orbits

In this section we study the map (3) with the force (4). We will think of Ω_2 primarily as a “structural parameter,” fixing it to be

$$\Omega_2 = \gamma \equiv \frac{1}{2}(\sqrt{5} - 1) \approx 0.618034, \quad (20)$$

the inverse of the golden mean. It is computationally infeasible to perform a detailed parameter study to determine how the dynamical behavior depends on all of the remaining parameters (Ω_1, a_1, a_2) . In most cases, we will study the dependence upon (Ω_1, a_1) for fixed a_2 , but in several cases we will instead fix a_1 and vary (Ω_1, a_2) .

⁴ Comparing WBA with Lyapunov in [9], gave a Hansen-Kuiper skill score $TSS = 0.997$. Comparing WBA or Lyapunov with 0–1 we found $TSS = 0.91$; this is lower because the inefficiency of the 0–1 test required us to reduce T to 1000.

⁵ The Kim-Ostlund tree can be used to get resonance relations [45]; however, it is not clear that this algorithm returns a minimal $\|m\|$.

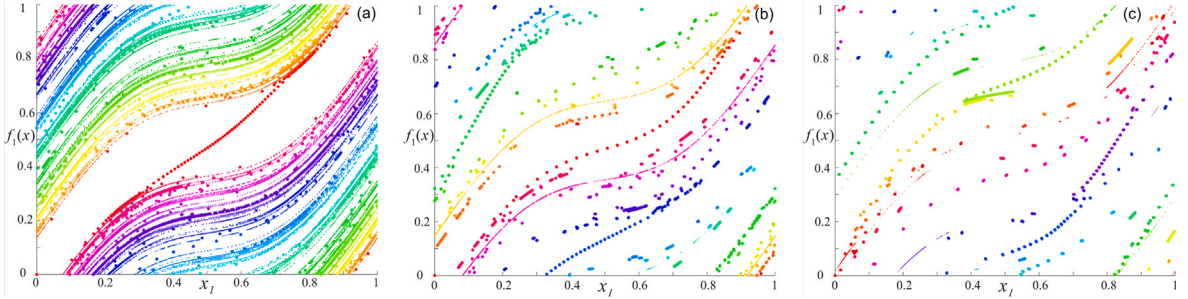


Fig. 1. Poincaré slices of regular orbits of the QPF circle map with $a_1 = 0.8$ and $\Omega_2 = \gamma$, for (a) $a_2 = 0.6$, (b) $a_2 = 2.49$ and (c) $a_2 = 5$ (these are the first, fourth, and eighth values in Fig. 8). The plot shows a grid of 200 values of $\Omega_1 \in [0, 1]$, with the orbits colored as in Fig. 2 using the value of ω_1 computed with $T = 10^6$. Resonant orbits are plotted with larger dots. Each orbit is iterated 10^5 times to remove transients, and the next 1000 points on the Poincaré slice $|x_2| < 0.0005$ are shown.

4.1. Regular orbits

Since the x_2 dynamics of (3) with (4) is a rigid rotation and $\omega_2 = \Omega_2 = \gamma$ is irrational, each orbit $\{(x_1(t), x_2(t)) : t \in \mathbb{N}\}$ is dense on $x_2 \in [0, 1]$. One way to visualize these dynamics is to take a Poincaré section, say at $x_2 = 0$; however, since the orbit is discrete we instead use a “Poincaré slice,” plotting points at a sequence of times t_j for which $|x_2(t_j)| < 0.0005$, see Fig. 1. In this figure we use the criterion (12) to select only the *nonchaotic* orbits, those for which the WBA has converged to at least nine digit accuracy, $\text{dig}_T \geq 9$, after $T = 10^6$ iterates. The vertical axis in the figure is the image

$$x_1(t_j + 1) = f_1(x_1(t_j), x_2(t_j)) \approx f_1(x_1(t_j), 0),$$

which, since $x_2 \approx 0$, is the Arnold function. Thus when a_2 is sufficiently small the resulting figure can be viewed as a perturbation of the one-dimensional Arnold map. Indeed, even when $a_2 = 0.6$, as in panel (a), the resulting orbits resemble those that one would see in Arnold’s map, and there are many regions with incommensurate frequency vectors (small dots), separated by resonant tongues, regions where $m \cdot \omega = n$ for some nonzero $(m, n) \in \mathbb{Z}^3$ (large dots), recall (14). Note that a resonant tongue corresponds to the existence of an attracting invariant circle on \mathbb{T}^2 . When $m_1 \neq 0$ and $m_2 \neq 0$ these resonances have irrational ω_1 :

$$\omega_1 = \frac{n}{m_1} - \frac{m_2}{m_1} \gamma \in \mathbb{R} \setminus \mathbb{Q}. \quad (21)$$

Computing the resonance order and using criterion (19) for Fig. 1(a), where $a_2 = 0.6$, we find ω is incommensurate for 26.7% of the orbits, while it is resonant for 72.3% (the remaining 1% are chaotic and not shown here). By contrast, in panel Fig. 1(b) where $a_2 = 2.49$, only 2% are incommensurate while 94.7% of the orbits are resonant (3.3% are chaotic). Finally for $a_2 = 5$ in panel (c), 1.1% are incommensurate, while 96.8% are resonant (2.1% are chaotic).

The rotation number ω_1 for nonresonant and resonant orbits is shown as a function of (Ω_1, a_1) in Fig. 2 for $a_2 = 0.6$ (top panels) and $a_2 = 1.0$ (bottom panels). These use a grid of 1000×1000 evenly spaced values of $(\Omega_1, a_1) \in [0, 1] \times [0, 2]$, with Ω_1 slightly shifted away from rationals to avoid resonances at $a_1 = 0$. Each orbit begins at the same randomly selected point $(x_1(0), x_2(0))$ and is initially iterated 10^4 times to remove transients. To compute both ω_T and dig_T we use $T = 10^6$. As noted by [1], the nonresonant regions (left panels) as a function of (Ω_1, a_1) , look similar to the circle map case when a_2 is small; however, the proportion of the nonresonant orbits appears to fall essentially to zero for a value of a_1 smaller than 1, unlike the Arnold case (more details are given in Section 6, below).

The parameters with resonant orbits are shown in Fig. 2(b) and (d) for the same values of a_2 . These are analogous to the tongues or mode-locking regions of the Arnold map; for example, the $\omega_1 = \frac{0}{1}$ (red), $\frac{1}{1}$ (red) and $\frac{1}{2}$ (cyan) tongues are prominent. However, rank-one resonances with $m_2 \neq 0$ (21) create additional tongues. Perhaps the most prominent new mode-locking regions are those with $(m_1, m_2, n) = (1, 1, 1)$, so that $\omega_1 = 1 - \gamma \approx 0.382$ (green) and with $(m_1, m_2, n) = (1, -1, 0)$ so that $\omega_1 = \gamma \approx 0.618$ (blue). Like the Arnold tongues, these have cusps when $a_1 = 0$ at $\Omega_1 = \omega_1$ and broaden as a_1 increases. However, unlike the Arnold map, these resonant regions do not monotonically increase in width when a_1 exceeds 1. These “leaf shaped” tongues were observed in [18].

An alternative view of the tongues is seen in Fig. 3, which shows the resonant regions for fixed $a_1 = 1.2$ on a 2000×2000 grid of $(\Omega_1, a_2) \in [0, 1] \times [0, 20]$. The larger tongues in the figure are labeled by the computed resonance vector (m_1, m_2, n) . Note that we can accurately compute these regions since, by (12), we find ω_1 with precision at least 10^{-9} . Feudel et al. [18] observed that for $a_1 = 1$ fixed, the widths of the tongues oscillate and narrow over intervals for $a_2 \in [0, 2\pi]$; this is referred to as *pinching*. In Fig. 3, some of the resonance tongues appear to pinch off completely, forming a sequence of “bubbles” or “isolas”. However, in general pinching does not require the width to become zero.

By contrast with our technique, Osinga et al. [3] computed the tongues using bifurcation curves, concentrating on the case $\omega_1 = 0$, i.e., $(m_1, m_2, n) = (1, 0, 0)$. For example, in [3, Fig. 2] they observe that when $a_1 = 0.8$ the first pinching occurs for $4.1 < a_2 < 4.8$; this corresponds to a region of bistability for several invariant circles. This pinching is reproduced in Fig. 3 for a similar range of a_2 , with $a_1 = 1.2$. Osinga et al. note that the formation of the pinches is associated with bifurcations in which a pair of invariant

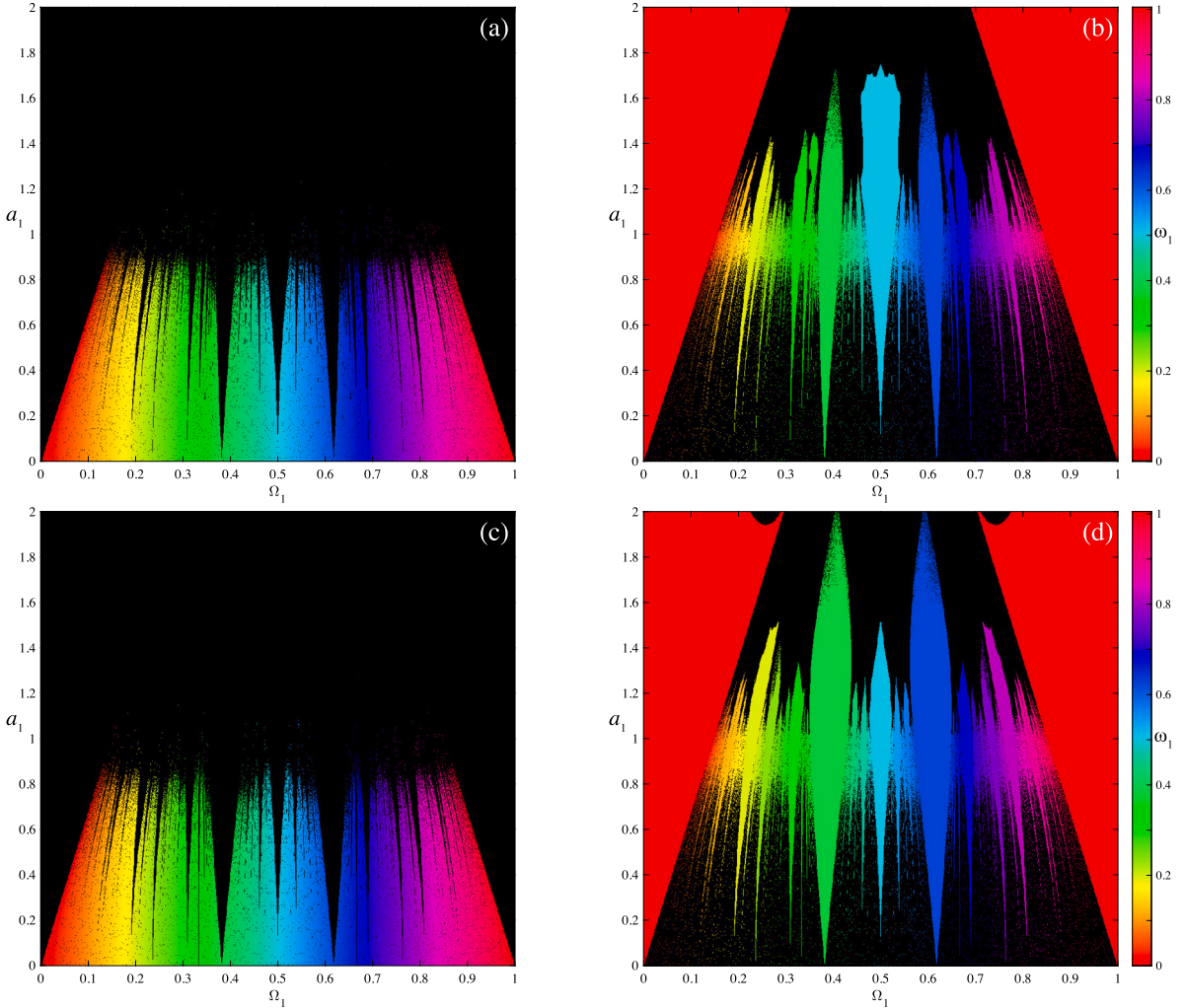


Fig. 2. Nonresonant (panels (a) and (c)) and resonant (panels (b) and (d)) orbits for the QPF circle map (4) as a function of (a_1, Ω_1) for $a_2 = 0.6$ (top panels) and $a_2 = 1$ (bottom panels), with $\Omega_2 = \gamma$ (20). These orbits are distinguished using (12) and (19). The orbits are colored using ω_1 as shown in the color bars. Black indicates no orbits of the given type.

circles collide at a dense set of points but the collision is not smooth. There can be multiple attracting orbits within a tongue and these can give rise to SNAs, see Section 5.

Glendinning et al. [46] show that the width of the $(1, 0, 0)$ resonance region is asymptotically $|J_0(a_2/(2 \sin(\pi\gamma)))|$, for $a_2 \gg 1$ and $a_1 \ll 1$. Here J_0 is the Bessel function; thus its zeros determine the pinching points in a_2 , and the width approaches zero as $\mathcal{O}(a_2^{-1/2})$ for large coupling. This formula predicts the first pinch at $a_2 = 4.48$. A similar result for $(m_1, m_2, n) = (1, -k, 0)$, involves the Bessel function J_k instead of J_0 , reflecting the zero width of these tongues at $a_2 = 0$. The actual bifurcations do not always pinch; they can have two or more folds bounding small regions of multi-stability—[3] shows that these correspond to saddle-node/pitchfork bifurcations of multiple circles.

Our computations are consistent with these previous results. For example, for $a_1 = 0.8$ (not shown), we observe that the $(1, 0, 0)$ tongue first pinches at $a_2 = 4.51$, though it does not pinch off completely. This tongue corresponds to the red region in Fig. 3. For this case $a_1 = 1.2$, and the first pinch point occurs at $a_2 = 4.40$ and the second at 9.63 . Note that our computations extend the previous results to larger values of a_2 , and we observe that the boundary of the tongue is not smooth as the Bessel function form would suggest: it has a number of cusps, most prominently for $a_2 \approx 8.5$. Indeed, most of the tongues in Fig. 3 have non-smooth boundaries for larger a_2 . For the $(2, 0, 1)$ tongue we observe pinch points at $(a_1, a_2) = (0.8, 2.04)$, $(0.8, 3.96)$, and $(1.2, 1.64)$. The $(3, 0, 1)$ tongue is significantly thinner for both a_1 values and is not labeled in Fig. 3; when $a_1 = 1.2$, its first pinch point occurs at $a_2 = 0.66$.

Most of the tongues considered previously correspond to the special case of $(m_1, 0, 1)$ resonances. However, as we see in Fig. 3, these are not the most prominent: they are only present for small a_2 and appear to disappear entirely as a_2 grows. We also observe that $m_2 \neq 0$ resonances are most prominent when $a_1 = 0.8$ (not shown). These additional tongues also often have shapes quite different from the $(1, 0, 0)$ tongue. For example, the $(1, -7, -4)$ tongue appears to increase in thickness with each oscillation, and

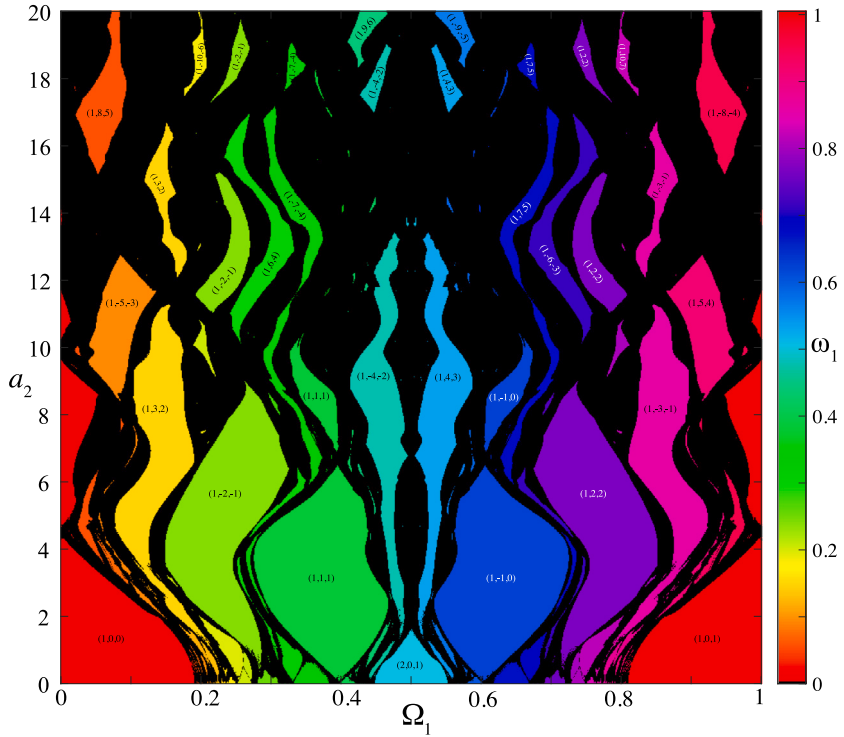


Fig. 3. Resonant regions for the QPF circle map (4) for $a_1 = 1.2$. The larger regions are labeled by (m_1, m_2, n) . Each resonance is colored by ω_1 and black regions correspond to either chaotic or incommensurate orbits.

therefore would not be well modeled by a Bessel function. The $(2, 0, 1)$ tongue does not have any apparent oscillation, but instead has a monotonically decreasing width as a_2 increases.

4.2. Chaos

Orbits identified as chaotic by the criterion (12) are shown in Figs. 4–5. Instead of using ω_1 for the color scheme — as we did in the previous figures — the colors in this figure indicate the Lyapunov exponent. For the nonlinearity (4) this is particularly easy to compute since the Jacobian of (3) is upper triangular:

$$Df = \begin{pmatrix} 1 + a_1 \cos(2\pi x_1) & a_2 \cos(2\pi x_2) \\ 0 & 1 \end{pmatrix}.$$

Since the lower right entry is 1, one of the multipliers is 1, and this implies that one of the Lyapunov exponents is zero. The other is simply the time average

$$\lambda = \lim_{t \rightarrow \infty} \frac{1}{t} \sum_{j=0}^{t-1} \ln |1 + a_1 \cos(2\pi x_1(j))|, \quad (22)$$

if this limit exists. Since (22) is the time average of a scalar function on phase space, we can also easily compute it using (8):

$$\lambda_T = WB_T(\ln |1 + a_1 \cos(2\pi x_1)|). \quad (23)$$

The average (23) was previously used in [21] to show that both Lyapunov exponents are zero for nonchaotic, nonresonant orbits of a torus map.

Of course, a weighted average like (23) should not be expected to improve convergence for orbits that are chaotic; however, when the orbit is periodic or quasiperiodic, we expect that λ_T should converge more rapidly than (22). Indeed our tests show that this is the case when $\lambda \leq 0$. For example, using a 500×500 portion of the grid in (Ω_1, a_1) , we find that when $a_2 = 0.6$ approximately 70% have $\lambda_T \leq 0$ for $T = 10^6$. For these regular cases, if we instead use a much smaller number of iterates, $T = 800$, we found the mean error $\langle \text{dig}_T \rangle = 3.6$ for (22), while $\langle \text{dig}_T \rangle = 7.9$ for (23). This more rapid convergence of (23) persists as T is increased.

Note that if $|a_1| > 1$ the function being averaged in (23) is not smooth, and since the weighted average relies on smoothness for improving convergence, we would not expect (23) to be helpful. Moreover, the only case for which the weighted average has been proven to be super-convergent is for orbits conjugate to a rigid quasiperiodic rotation [47]: there are no such orbits when $|a_1| > 1$. Nevertheless the less accurate computations of the Lyapunov exponent still do indicate that $\lambda_T > 0$ for many orbits as a_1 grows

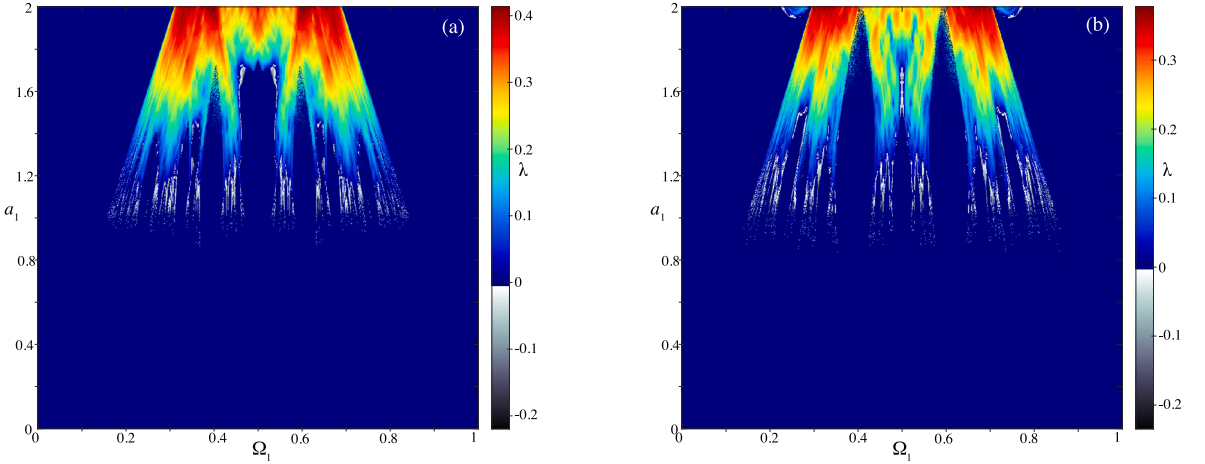


Fig. 4. Chaotic orbits of the QPF circle map (4) for a 1000×1000 grid in the (Ω_1, a_1) plane for (a) $a_2 = 0.6$ and (b) $a_2 = 1$. The color bar corresponds to λ_T (23). Parameters with $\lambda_T \leq 0$ are gray; they correspond to weak chaos, or strange nonchaotic attractors. Parameters with nonchaotic orbits are colored dark blue, and strongly chaotic orbits have colors that vary with λ_T .

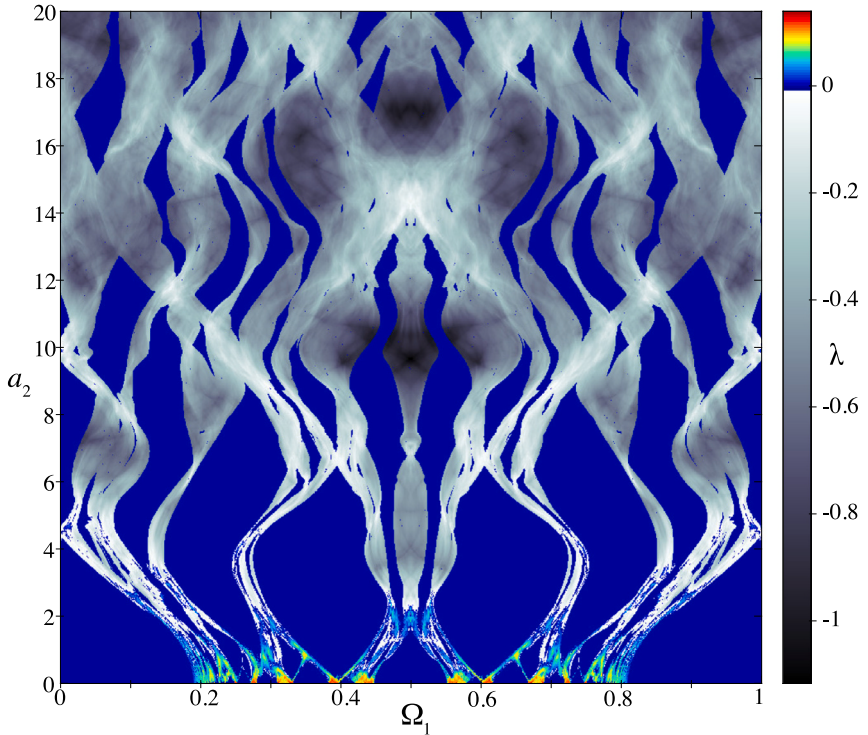


Fig. 5. Quasiperiodically-forced circle map (4) for $a_1 = 1.2$ for a 1000×1000 grid in (Ω_1, a_2) showing orbits with sensitive dependence using Criterion (11), colored by Lyapunov exponent (23). The grayscale indicates strange nonchaotic attractors. Blue indicates nonchaotic parameters, most of which correspond to the resonance regions in Fig. 3.

in Fig. 4. There are also orbits in these panels that are chaotic according to (11), but for which $\lambda_T \leq 0$ —they are shown in gray in Figs. 4–5; that is, these gray points are points for which WBA chaos, a measure of sensitive dependence on initial conditions, disagrees with Lyapunov exponent chaos, a measure of local stretching of the linearization. We discuss this further in the next section.

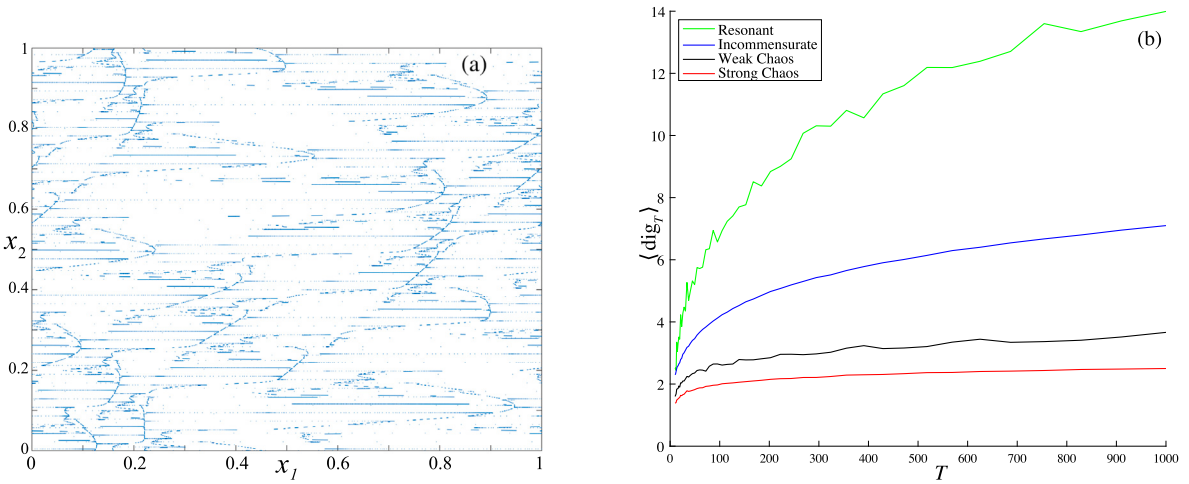


Fig. 6. (a) A phase portrait of a weakly chaotic orbit for (4) with $(a_1, a_2) = (0.93493, 1)$ and $\Omega_1 = 0.5526$. (b) The mean value of dig_T as a function of $T \in [0, 1000]$ for (4) with $a_1 \in [0, 2]$, $a_2 = 1$ and $\Omega_1 \in [0, 1]$. The orbits are separated into four types: strongly chaotic orbits have the smallest $\langle \text{dig}_T \rangle$ (red), followed by weakly chaotic orbits (black), nonresonant (blue), and finally resonant orbits (green). Out of the 10^6 orbits sampled, 4213 were identified as weakly chaotic. For comparison we randomly selected 4213 orbits of each of the other types.

5. Weak chaos

It was first observed in [1] that there is a range around $a_1 = 1$ for which QPF circle maps can exhibit strange nonchaotic attractors (SNAs), defined as attractors that are geometrically strange, but which have $\lambda \leq 0$. While this is a compelling idea, it was noted in [2] that: “The nature of this definition makes it impossible to prove strangeness based solely on a computer simulation.”

Instead, of this definition of SNAs, we use the notion of “weak chaos”: sensitive dependence on initial conditions that does not correspond to an exponential instability. Thus we identify SNAs as invariant sets for which the WBA converges slowly—hence are not regular—but for which the Lyapunov exponent is not positive—hence are not strongly chaotic. In particular, the criterion (11) combined with negative Lyapunov exponent serves as our new criterion for weak chaos/SNA:

$$\text{dig}_T < D_T \text{ and } \lambda_T \leq 0 \Rightarrow \text{“weakly chaotic”}. \quad (24)$$

Alternatively when $\lambda_T > 0$ we refer to the orbit as having “strong chaos”, or — more simply — as chaotic. The criterion (24) gives an efficient way to distinguish between these classes of orbits, and agrees with the results of [7] that showed that some cases of SNAs do correspond to weak chaos.

As mentioned in the previous section, the gray points in Fig. 4 are points with weak chaos. Panel (a) of this figure is more detailed than but in agreement with Fig. 1 of [1]. Panel (b) shows that weak chaos appears for a larger range of a_1 for $a_2 = 1$. In both cases, for fixed a_1 in a range around 1, the zone of weak chaos appears to be a Cantor set-like region. In order to get a more complete understanding of the scope of weak chaos, in Fig. 5 we fix $a_1 = 1.2$, and allow a_2 to vary between 0 and 20. This figure shows that as a_2 grows large, there are no visible regions of strong chaos, but a significant positive measure portion of the parameter space exhibits weak chaos.

An example is shown in Fig. 6(a); this is an orbit of (3) with (4) that has $\text{dig}_T = 8.4 < D_T$ and $\lambda_T = -0.0648 < 0$ so, using (12), it satisfies (24) for $T = 10^6$. Visually, the phase portrait shows the expected geometric “strangeness”. Since we use the convergence rate of the WBA to detect chaos and not the geometry of the orbit, our criterion (24) differs significantly from previously used methods to identify SNAs.

For the example in Fig. 6(a), $|a_1| < 1$ so the rotation number does exist and is independent of initial condition; however, as was emphasized in [14] the convergence of (2) can be slower than T^{-1} for such weakly chaotic orbits. Stark et al. constructed an algorithm that is guaranteed to converge as T^{-1} by averaging over initial conditions. To compute this, they use a discrete approximation to the integral on a grid $x_2(0) = \frac{i}{N}$, $i = 0, \dots, N$, to obtain

$$\omega_1^{Stark} = \frac{1}{NT} \sum_{i=0}^{N-1} \left(f^T(x_1, \frac{i}{N}) - (x_1, \frac{i}{N}) \right). \quad (25)$$

For example, when $(a_1, a_2) = (0.8, 6\pi)$, and $\Omega_1 = 0.01$, the map has an SNA according to [13]. Using $N = 10^3$ and $T = 10^5$, in (25), [14] computed

$$\omega_1^{Stark} = 0.0173598.$$

When we use (13) to compute ω_T with $T = 10^6$ we obtain the same value to the quoted accuracy, and find $\text{dig}_T = 6.4$, which is consistent with six digits accuracy. For this case, $\lambda_T = -0.2646098$, so by Criterion (24) this orbit is indeed weakly chaotic. This example, and others that we have tried, show that the WBA can give the same accuracy as (25) with a factor of 50 fewer iterates!

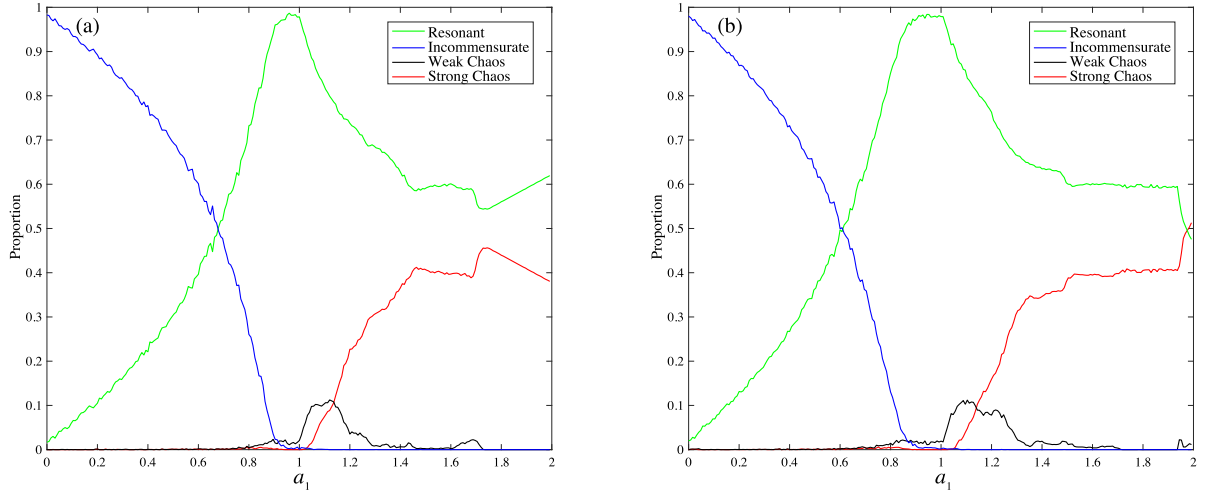


Fig. 7. The proportion of strongly chaotic (red), weakly chaotic (black), resonant (green), and incommensurate (blue) orbits for (3) with (4) as a function of a_1 . (a) $a_2 = 0.6$ and (b) $a_2 = 1$.

We show in Fig. 6(b) that there are distinct differences in the number of digits, dig_T , for the four categories of orbits: resonant, incommensurate, weakly chaotic, and strongly chaotic. Here we selected orbits from the data in Fig. 2 and Fig. 4 with $a_2 = 1$. Of the 10^6 orbits, 4213 were identified as weakly chaotic using (24). The black curve in the figure shows the average $\langle \text{dig}_T \rangle$ for these orbits as a function of T . For a fairer comparison, we randomly selected the same number of orbits of the other three types. Note that for each T in Fig. 6(b), $\langle \text{dig}_T \rangle$ is ordered monotonically by type; it is largest for the resonant orbits, smaller for the incommensurate case, smaller for weak chaos and finally smallest for strong chaos. In particular, ω_T for the resonant orbits nearly reaches double precision accuracy (at least in the mean) even for $T = 1000$. In addition, the rate of increase of dig_T with T is also ordered in the same way by type; however, the distinction in rates between the weakly and strongly chaotic orbits is less pronounced. Nevertheless, even though these distinctions are clear for the average $\langle \text{dig}_T \rangle$, this method does not give a reliable classification: the values of dig_T for individual orbits can vary significantly.

6. Orbit-type statistics

The proportions of orbits of each of the four types — strongly chaotic (red), weakly chaotic (black), resonant (green) and incommensurate (blue) — are shown in Fig. 7. This figure uses the data in Figs. 2 and 4, summed over Ω_1 , as a function of a_1 for two fixed values of a_2 .

Note that the curves for the incommensurate orbits (blue) should begin at 1 when $a_1 = 0$ according to (6); however, our method underestimates this fraction by about 1.5%, declaring that orbits with orders outside the interval (19) are resonant. Some cutoff is inevitable, of course, since we cannot compute with infinite precision; moreover, a given precision δ results on average in a smaller resonance order in higher dimensions: compare the factor of $\frac{1}{3}$ in (18) with the factor $\frac{1}{2}$ for the 1D case in [9]. The incommensurate fraction in Fig. 7 drops nearly to zero with a shape similar to the power law behavior seen for a circle map [48,49], but in contrast to the 1D case, it becomes nearly zero at a value $a_1 < 1$. The onset of weak chaos (black curves) is just below this point. Of course, when $a_1 > 1$, there are no incommensurate orbits, and our method falsely identifies very few.

The fraction of resonant orbits (green) no longer has the cusp at $a_1 = 1$ that is seen for a circle map [49], and it now decreases more substantially when $a_1 > 1$. This, of course could be anticipated from the right panels of Fig. 2, since the widths of some of the resonant tongues decrease for $a_1 > 1$.

The onset of weakly chaotic orbits (black) occurs near $a_1 = 0.74$ for $a_2 = 0.6$, and it has a peak of about 10% for $a_1 \in (1.05, 1.15)$. For panel (b), where $a_2 = 1$, the onset is near $a_1 = 0.66$, and the peak proportion has the same height but is broader. In both cases the weakly chaotic proportion is nonzero up to $a_1 \approx 1.7$.

The chaotic fraction in Fig. 7 (red) is nonzero for $a_1 > 1$ and grows to about 40% when $a_1 = 2$, which is larger than that found for a circle map [49]. In panel (a), the chaotic fraction appears to reach a peak and then decrease as it does for the circle map. We conjecture that the same would be true in panel (b), but that the peak occurs for $a_1 > 2$.

Fig. 8(a) gives an overview of how the chaotic fraction varies with all three parameters, a_1 , a_2 , and Ω_1 . In this figure, parameters exhibiting strong chaos are red and those with weak chaos are black. The remaining white regions contain resonant and incommensurate orbits. This data is shown for eight values of $a_2 \in [0.6, 5]$ (vertical axis) as a function of $(\Omega_1, a_1) \in [0, 1] \times [0.6, 2]$ (horizontal axes). This three-dimensional view of the data extends the views in Fig. 2 and Fig. 4, which fix a_2 and plot (Ω_1, a_1) , and Fig. 3 and Fig. 5, which fix a_1 and plot (Ω_1, a_2) .

A striking feature of Fig. 8(a) is the change in the relative proportions of strong and weak chaos as the parameters vary. Recall that Fig. 5 — essentially a vertical slice of Fig. 8(a) for $a_1 = 1.2$ — showed that when $a_2 \gtrsim 8$ the proportion of weak chaos increases

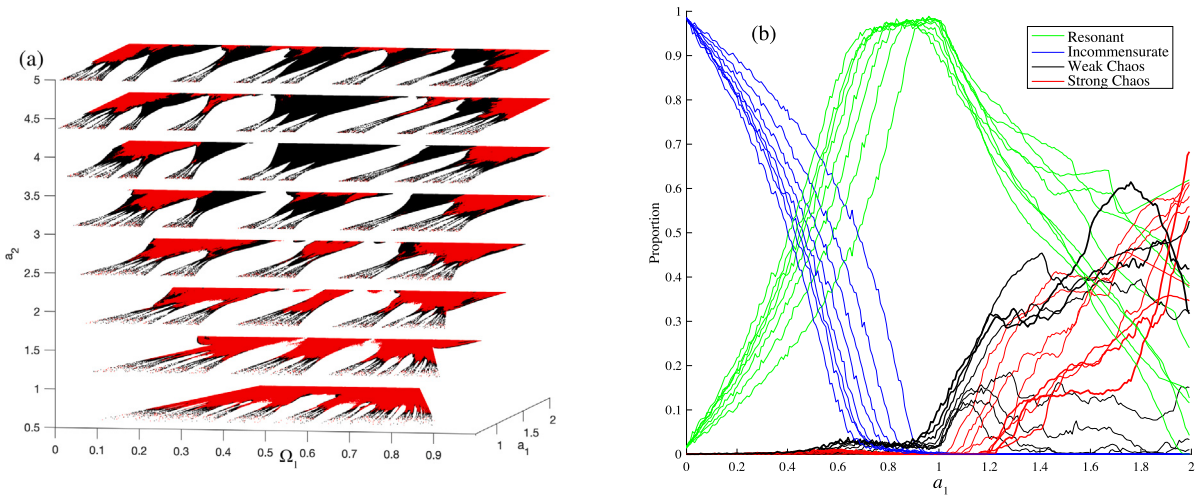


Fig. 8. Types of orbits for a grid of eight $a_2 \in [0.6, 5]$ as a function of (a_1, Ω_1) for (3) with (4). (a) Parameter regions with strongly (red) and weakly (black) chaotic orbits. The range $a_1 \in (0.6, 2)$ is shown since the chaotic fractions are negligible for smaller a_1 values. (b) Proportion of the four orbit types as a function of a_1 for each of the eight a_2 values of panel (a) using the color scheme of Fig. 7. The thickness of the eight curves increases with a_2 .

significantly, especially near $\Omega_1 \approx 0.5$. This large fraction is echoed in Fig. 8(a) for other values of a_1 as well. Alternatively, slices of Fig. 8(a) for constant a_2 were seen in Fig. 4. These slices, for $a_2 = 0.6$ and 1, indicate that for smaller a_2 , weak chaos is primarily confined to a small region near $a_1 = 1$ and to small Cantor set-like intervals in Ω_1 . Fig. 8(a) makes it clear that this structure near $a_1 = 1$ persists as a_2 grows, though the thickness of the weakly chaotic intervals increases with a_2 .

The proportion of the four orbit types as a function of a_1 is shown in Fig. 8(b) for each of the eight values of a_2 from panel (a). For panel (b), increasing thickness of the curves is used to indicate increasing values of a_2 . These curves summarize the trends from panel (a). For each a_2 , the fraction of incommensurate orbits (blue curves) is underestimated when $a_1 = 0$ by about 1.5%, just as we noted for Fig. 7. As a_1 grows this fraction decreases (nearly) monotonically for each a_2 . Recall from Fig. 2(a)–(c), that the incommensurate orbits seem to disappear just below $a_1 = 1$. This is also reflected in Fig. 8(b) for each curve: the incommensurate fraction drops rapidly, nearly — but not quite — reaching zero for $a_1 \in (0.65, 0.95)$, and the value at which this occurs decreases monotonically with a_2 . After a further slower decrease with a_1 , these fractions necessarily hit zero when $a_1 = 1$, where the map loses invertibility. Recall that the similar curves for circle maps have a universal power law form [48]. There appears to be no such universal law for these QPF maps.

The value of a_1 at which the incommensurate fraction nearly reaches zero in Fig. 8(b) is close to the point at which weakly chaotic orbits (black curves) first appear. For $a_1 > 1$, the fraction of weak chaos increases as a_2 increases. Note also that the fraction of weak chaos for each fixed a_2 reaches a peak as a_1 grows, and decays thereafter. This peak reaches 60% for $(a_1, a_2) \approx (1.75, 5)$. The chaotic fraction (red curves) also grows with a_1 , but for the larger values of a_2 , this fraction is below that of the weakly chaotic orbits.

The increasing chaotic fraction is at the expense of the resonant orbits (green curves): each of these peaks near $a_1 = 1$ and decreases roughly monotonically thereafter. As a_2 grows, resonant fraction appears to decrease, this is also seen in Fig. 8(a) for largest values, $a_1 = 2$ and $a_2 = 5$. Indeed, the resonant proportion in panel (b) for the largest $a_2 = 5$, (the thickest green curve) reaches nearly zero as a_1 nears 2. This agrees with the shrinking tongue widths seen in Fig. 2(b) and (d).

7. Conclusions

In this paper, we used efficient, high-precision numerical techniques to characterize the dynamics of a quasiperiodically-forced (QPF) extension of the Arnold circle map. We used the weighted Birkhoff average (WBA) (8) to distinguish between chaotic and regular orbits by defining a threshold for the precision, dig_T (10), after a fixed number of iterates T . An advantage of the WBA is that it can rapidly compute the rotation vector, as well as the time average of other phase space functions [9,10], to near machine precision when the orbit is regular: it is super-convergent when the orbit is smoothly conjugate to a rigid rotation with Diophantine vector [47]. We observed that the computations are even more rapidly convergent when the rotation vector is resonant, recall Fig. 6(b).

Given an accurate value for rotation vector ω_T (13), we determined if the vector is nearly resonant by finding the smallest order of an integer resonance plane within a distance δ . Since we know the precision of the rotation vector is at least 10^{-9} we chose this value for δ . This allowed us to characterize regular orbits as incommensurate (nonresonant) or rank-one (resonant). We used a similar, but more efficient method — based on the Farey tree — for a scalar frequency in [9]. We hope that an efficient algorithm to compute (17) for higher dimensional cases can be found. Meanwhile, we used a brute force method, following our previous work

on volume-preserving maps [10]. The (m_1, m_2, n) resonances correspond to the generalization of Arnold tongues to the QPF case, recall Fig. 3.

Using these methods, we were able to efficiently classify the trajectories of QPF circle maps into four categories: resonant, incommensurate, weakly chaotic, and strongly chaotic, and — as in Figs. 7–8 — showed how their proportions vary with the strength of the nonlinearity. With this ability to characterize the behavior of orbits for a large parameter region, we have been able to compute generalized Arnold tongues for larger parameter ranges and higher-order resonances than before. We observed in Fig. 3 that the pinching of these as a function of the coupling parameter, a_2 , which has been previously reported for low-order resonances, also occurs at higher orders as well as for nonzero m_2 . We could observe a wider variety of types of pinching than had been seen previously, including cases with no oscillations, and cases where the oscillating tongues increase in width rather than decay in width.

Using our modified definition of strange nonchaotic attractors (SNAs) as orbits that are actually “weakly chaotic”, we showed in Fig. 5 that a relatively large parameter region exhibits SNAs as the coupling, a_2 , becomes large. The variation in the weakly chaotic fraction as a function of the nonlinear amplitude, a_1 shown in Fig. 8 indicates that such orbits can become the majority for larger coupling.

There are a number of future questions that remain, a couple of which we have considered elsewhere. In this paper, we have shown that the WBA can also be used to improve the accuracy of Lyapunov exponents over the simplest averaging method (22)—though this does not give the super-convergence seen for Diophantine rotations. We investigate the computation of Lyapunov exponents in more detail in [50]. Furthermore, this study of QPF circle maps is only a first step towards understanding full two-dimensional torus maps. We have considered the application of these methods to these maps in [49]. There are other areas which we could address in the future. For example, we have used WBA to study tongues and weak chaos, whereas others have used continuation methods to study the bifurcations leading to such behavior. An interesting follow-up would be to combine these two methods in order to get both a global picture of behavior, as well as a more thorough understanding of the underlying dynamics that lead to the classes of orbits that we observe.

CRediT authorship contribution statement

J.D. Meiss: Writing – review & editing, Writing – original draft, Software, Methodology, Investigation, Formal analysis, Conceptualization. **E. Sander:** Writing – review & editing, Writing – original draft, Software, Methodology, Investigation, Formal analysis, Conceptualization.

Declaration of competing interest

The authors declare the following financial interests/personal relationships which may be considered as potential competing interests: James D. Meiss reports financial support was provided by Simons Foundation under Award 601972. Evelyn Sander reports financial support was provided by Simons Foundation under Award 636383. They declare that they have no known competing financial interests or personal relationships that could have appeared to influence the work reported in this paper.

Data availability

Data will be made available on request.

References

- [1] Ding M, Grebogi C, Ott E. Evolution of attractors in quasiperiodically forced systems: From quasiperiodic to strange nonchaotic to chaotic. *Phys Rev* 1989;39A(5):2593–8. <http://dx.doi.org/10.1103/physreva.39.2593>.
- [2] Sturman R. Scaling of intermittent behaviour of a strange nonchaotic attractor. *Phys Lett A* 1999;259:355–65. [http://dx.doi.org/10.1016/S0375-9601\(99\)00463-6](http://dx.doi.org/10.1016/S0375-9601(99)00463-6).
- [3] Osinga H, Wiersig J, Glendinning P, Feudel U. Multistability in the quasiperiodically forced circle map. *Int J Bifurcation Chaos* 2001;11(12):3085–105. <http://dx.doi.org/10.1142/S0218127401004029>.
- [4] Glendinning P, Jäger TH, Stark J. Strangely dispersed minimal sets in the quasiperiodically forced Arnold circle map. *Nonlinearity* 2009;22:835–54. <http://dx.doi.org/10.1088/0951-7715/22/4/008>.
- [5] Herman MR. Une méthode pour minorer les exposants de Lyapounov et quelques exemples montrant le caractère local d'un théorème d'Arnold et de Moser sur le tore de dimension 2. *Comment Math Helv* 1983;58:453–502. <http://dx.doi.org/10.1007/BF02564647>.
- [6] Grebogi C, Ott E, Pelikan S, Yorke JA. Strange attractors that are not chaotic. *Phys D* 1984;13:261–8. [http://dx.doi.org/10.1016/0167-2789\(84\)90282-3](http://dx.doi.org/10.1016/0167-2789(84)90282-3).
- [7] Glendinning P, Jäger TH, Keller G. How chaotic are strange non-chaotic attractors? *Nonlinearity* 2006;19:2005–22. <http://dx.doi.org/10.1088/0951-7715/19/9/001>.
- [8] Duignan N, Meiss JD. Distinguishing between regular and chaotic orbits of flows by the weighted Birkhoff average. *Phys D* 2023;449(July):133749. <http://dx.doi.org/10.1016/j.physd.2023.133749>.
- [9] Sander E, Meiss JD. Birkhoff averages and rotational invariant circles for area-preserving maps. *Phys D* 2020;411:132569. <http://dx.doi.org/10.1016/j.physd.2020.132569>.
- [10] Meiss JD, Sander E. Birkhoff averages and the breakdown of invariant tori in volume-preserving maps. *Phys D* 2021;428(15):133048. <http://dx.doi.org/10.1016/j.physd.2021.133048>.
- [11] Katok AB, Hasselblatt B. *Introduction to the modern theory of dynamical systems*. In: *Encyclopedia of mathematics and its applications*, vol. 54, Cambridge: Cambridge University Press; 1995.

- [12] Guckenheimer J, Holmes P. Nonlinear oscillations, dynamical systems, and bifurcations of vector fields. In: Appl. math. sci., vol. 42, New York: Springer-Verlag; 2002, <http://dx.doi.org/10.1007/978-1-4612-1140-2>.
- [13] Feudel U, Kurths J, Pikovsky A. Strange non-chaotic attractor in a quasiperiodically forced circle map. Phys D 1995;88:176–86. [http://dx.doi.org/10.1016/0167-2789\(95\)00205-1](http://dx.doi.org/10.1016/0167-2789(95)00205-1).
- [14] Stark J, Feudel U, Glendinning P, Pikovsky A. Rotation numbers for quasiperiodically forced monotone circle maps. Dyn Syst 2002;17:1–28. <http://dx.doi.org/10.1080/14689360110073641>.
- [15] Kim JW, Kim SY, Hunt B, Ott E. Fractal properties of robust strange nonchaotic attractors in maps of two or more dimensions. Phys Rev E 2003;67(3):036211. <http://dx.doi.org/10.1103/PhysRevE.67.036211>.
- [16] Jäger TH, Stark J. Towards a classification for quasiperiodically forced circle homeomorphisms. J Lond Math Soc 2006;73(2):727–44. <http://dx.doi.org/10.1112/S00246107060022782>.
- [17] Bjerklov K, Jäger TH. Rotation numbers for quasiperiodically forced circle maps—Mode-locking vs string monotonicity. J Amer Math Soc 2009;22:353–62, <https://www.jstor.org/stable/40587236>.
- [18] Feudel U, Grebogi C, Ott E. Phase-locking in quasiperiodically forced systems. Phys Rep 1997;290:11–25. [http://dx.doi.org/10.1016/S0370-1573\(97\)00055-0](http://dx.doi.org/10.1016/S0370-1573(97)00055-0).
- [19] Das S, Dock CB, Saiki Y, Salgado-Flores M, Sander E, Wu J, Yorke JA. Measuring quasiperiodicity. Euro Phys Lett 2016;114:40005. <http://dx.doi.org/10.1209/0295-5075/114/40005>.
- [20] Das S, Saiki Y, Sander E, Yorke JA. Quasiperiodicity: Rotation numbers. In: Skladas C, editor. Foundations of chaos revisited: from Poincaré to recent advancement. Understanding complex systems, Springer; 2016, p. 103–18. http://dx.doi.org/10.1007/978-3-319-29701-9_7.
- [21] Das S, Saiki Y, Sander E, Yorke JA. Quantitative quasiperiodicity. Nonlinearity 2017;30(11):4111. <http://dx.doi.org/10.1088/1361-6544/aa84c2>.
- [22] Das S, Saiki Y, Sander E, Yorke JA. Solving the babylonian problem of quasiperiodic rotation rates. Discrete Contin Dyn Syst 2019;12(8):2279–305. <http://dx.doi.org/10.3934/dcdss.2019145>.
- [23] Kachurovskii AG. The rate of convergence in ergodic theorems. Russian Math Surveys 1996;51(4):653. <http://dx.doi.org/10.1070/RM1996v05n04ABEH002964>.
- [24] Krengel U. On the speed of convergence in the ergodic theorem. Monatshefte Math 1978;86:3–6. <http://dx.doi.org/10.1007/BF01300052>.
- [25] Ruth M, Bindel D. Finding Birkhoff averages via adaptive filtering. Chaos 2024;34(12):123109, <http://dx.doi.org/10.1063/5.0215396>.
- [26] Tong Z, Li Y. Exponential convergence of the weighted Birkhoff average. J Math Pures Appl 2024;188:470–92. <http://dx.doi.org/10.1016/j.matpur.2024.06.003>.
- [27] Chen HY, Haynes AL. Expected value of the smallest denominator in a random interval of fixed radius. Int J Number Theory 2023. <http://dx.doi.org/10.1142/S1793042123500689>.
- [28] Marklof J. The log moments of smallest denominators. Zenodo 2024;24(June):1–13. <http://dx.doi.org/10.5281/zenodo.12167470>.
- [29] Marklof J. Smallest denominators. Bull Lond Math Soc 2024;56(6):1920–38, <https://londmathsoc.onlinelibrary.wiley.com/doi/10.1112/blms.13034>.
- [30] Szczepach JD, Lopes SR, Viana RL. Finite-time Lyapunov spectrum for chaotic orbits of non-integrable Hamiltonian systems. Phys Lett A 2005;335(5–6):394–401. <http://dx.doi.org/10.1016/j.physleta.2004.12.058>.
- [31] Gottwald GA, Melbourne I. On the implementation of the 0–1 test for chaos. SIAM J Appl Dyn Syst 2009;8(1):129–45. <http://dx.doi.org/10.1137/080718851>.
- [32] Alsedà L, Borrós-Cullell S. An algorithm to compute rotation intervals of circle maps. Commun Nonlinear Sci Numer Simulat 2021;102:105915. <http://dx.doi.org/10.1016/j.cnsns.2021.105915>.
- [33] Polotzek K, Padberg-Gehle K, Jäger TH. Set-oriented numerical computation of rotation sets. J Comput Dyn 2017;4(1–2):119–41. <http://dx.doi.org/10.3934/jcd.2017004>.
- [34] Sanchez J, Net M, Simo C. Computation of invariant tori by Newton–Krylov methods in large-scale dissipative systems. Phys D 2010;239(3):123–33. <http://dx.doi.org/10.1016/j.physd.2009.10.012>.
- [35] Haro A, Canadell M, Figueras JL, Josep AL, Mondelo M. The Parameterization Method for Invariant Manifolds. From Rigorous Results to Effective Computations. Springer International; 2016, <http://dx.doi.org/10.1007/978-3-319-29662-3>.
- [36] Blessing D, James JDM. Weighted Birkhoff averages and the parameterization method. SIAM J. Dyn. Syst. 2024;23(3):1766–804, <http://dx.doi.org/10.1137/23M1579546>.
- [37] Laskar J. Frequency analysis for multi-dimensional systems. Global dynamics and diffusion. Phys D 1993;67:257–83. [http://dx.doi.org/10.1016/0167-2789\(93\)90210-R](http://dx.doi.org/10.1016/0167-2789(93)90210-R).
- [38] Laskar J. Frequency map analysis and particle accelerators. In: Proceedings of the 2003 IEEE particle accelerator conference (pac 03). IEEE; 2003, p. 378–82. <http://dx.doi.org/10.1109/PAC.2003.1288929>.
- [39] Seara TM, Villanueva J. On the numerical computation of Diophantine rotation numbers of analytic circle maps. Phys D 2006;217(2):107–20. <http://dx.doi.org/10.1016/J.Physd.2006.03.013>.
- [40] Luque A, Villanueva J. Computation of derivatives of the rotation number for parametric families of circle diffeomorphisms. Phys D 2008;237(20):25992615. <http://dx.doi.org/10.1016/j.physd.2008.03.047>.
- [41] Seara TM, Villanueva J. Numerical computation of the asymptotic size of the rotation domain for the Arnold family. Phys D 2009;238(2):197–208. <http://dx.doi.org/10.1016/J.Physd.2008.09.002>.
- [42] Luque A, Villanueva J. Quasi-periodic frequency analysis using averaging-extrapolation methods. SIAM J Dyn Syst 2014;13(1):1–46. <http://dx.doi.org/10.1137/130920113>.
- [43] Villanueva J. A new averaging-extrapolation method for quasi-periodic frequency refinement. Phys D 2022;438:133344. <http://dx.doi.org/10.1016/j.physd.2022.133344>.
- [44] Bazzani A, Giovannozzi M, Montanari CE, Turchetti G. Performance analysis of indicators of chaos for nonlinear dynamical systems. Phys Rev E 2023;107(6):064209. <http://dx.doi.org/10.1103/PhysRevE.107.064209>.
- [45] Ashwin P, Guaschi J, Phelps JM. Rotation sets and phase-locking in an electronic three oscillator system. Phys D 1993;66(3–4):392–411. [http://dx.doi.org/10.1016/0167-2789\(93\)90075-C](http://dx.doi.org/10.1016/0167-2789(93)90075-C).
- [46] Glendinning P, Feudel U, Pikovsky AS, Stark J. The structure of mode-locked regions in quasi-periodically forced circle maps. Phys D 2000;140:227–43. [http://dx.doi.org/10.1016/S0167-2789\(99\)00235-3](http://dx.doi.org/10.1016/S0167-2789(99)00235-3).
- [47] Das S, Yorke JA. Super convergence of ergodic averages for quasiperiodic orbits. Nonlinearity 2018;31(2):491–501. <http://dx.doi.org/10.1088/1361-6544/aa99a0>.
- [48] Ecke RE, Farmer JD, Umberger DK. Scaling of the Arnold tongues. Nonlinearity 1989;2:175–96. <http://dx.doi.org/10.1088/0951-7715/2/2/001>.
- [49] Sander E, Meiss JD. Proportions of incommensurate, resonant, and chaotic orbits for torus maps. 2024, submitted for publication, <https://arxiv.org/abs/2407.12039>.
- [50] Sander E, Meiss JD. Computing Lyapunov exponents using weighted Birkhoff averages. 2024, submitted for publication, <https://arxiv.org/abs/2409.08496>.